JGR Space Physics

RESEARCH ARTICLE
10.1029/2018JA026067

How Well Can We Estimate Pedersen Conductance From the THEMIS White-Light All-Sky Cameras?

M. M. Lam[1], M. P. Freeman[2], C. M. Jackman[1], I. J. Rae[3], N. M. E. Kalmoni[3], J. K. Sandhu[3], and C. Forsyth[3]

[1]Department of Physics and Astronomy, University of Southampton, Southampton, UK, [2]British Antarctic Survey, Cambridge, UK, [3]Mullard Space Science Laboratory, University College London, London, UK

Key Points:
- We use a white-light all-sky imager to estimate Pedersen conductance to within an uncertainty of 3 mho or 40%
- We relate Pedersen conductance to the optical intensity with a single parabolic relationship across a wide range of geomagnetic activity
- Our results enable the exploitation of white-light camera networks to study continental-scale phenomena such as substorms

Supporting Information:
- Supporting Information S1

Correspondence to:
M. M. Lam,
maimailam7@gmail.com

Citation:
Lam, M. M., Freeman, M. P., Jackman, C. M., Rae, I. J., Kalmoni, N. M. E., Sandhu, J. K., & Forsyth, C. (2019). How well can we estimate Pedersen conductance from the THEMIS white-light all-sky cameras? *Journal of Geophysical Research: Space Physics*, *124*. https://doi.org/10.1029/2018JA026067

Received 6 SEP 2018
Accepted 6 MAR 2019
Accepted article online 12 MAR 2019

Abstract We show that a white-light all-sky imager can estimate Pedersen conductance with an uncertainty of 3 mho or 40%. Using a series of case studies over a wide range of geomagnetic activity, we compare estimates of Pedersen conductance from the backscatter spectrum of the Poker Flat Incoherent Scatter Radar with auroral intensities. We limit this comparison to an area bounding the radar measurements and within a limited area close to (but off) imager zenith. We confirm a linear relationship between conductance and the square root of auroral intensity predicted from a simple theoretical approximation. Hence, we extend a previous empirical result found for green-line emissions to the case of white-light off-zenith emissions. The difference between the radar conductance and the best-fit relationship has a mean of -0.76 ± 4.8 mho and a relative mean difference of $21\% \pm 78\%$. The uncertainties are reduced to -0.72 ± 3.3 mho and $0\% \pm 40\%$ by averaging conductance over 10 min, which we attribute to the time that auroral features take to move across the imager field being greater than the 1-min resolution of the radar data. Our results demonstrate and calibrate the use of Time History of Events and Macroscale Interactions during Substorms all-sky imagers for estimating Pedersen conductance. This technique allows the extension of estimates of Pedersen conductance from Incoherent Scatter Radars to derive continental-scale estimates on scales of ~1–10 min and ~100 km^2. It thus complements estimates from low-altitude satellites, satellite auroral imagers, and ground-based magnetometers.

Plain Language Summary The Sun is a rotating magnetic plasma ball that releases energetic charged particles and magnetism in a "solar wind." Sometimes, this wind "shakes hands" with the Earth's magnetic field, allowing energy to be pumped into region near the Earth, stretching magnetic field lines like an elastic band. Much energy is released explosively in a "substorm" causing complex and brilliant auroral light displays about the size of a continent. This can be examined really well over several kilometers by radars on the ground. However, the radars cannot tell you what is happening for the whole substorm which is the size of a continent. It had been suggested that you can use a surface camera with a filter on it to estimate the part of the conductivity that tells us how much electric currents are heating the atmosphere. We asked whether the network of nonfiltered cameras stretching across North America could measure the conductivity as well as a radar can. We found they do half as well as the radar. This means we can use this camera network and its data archive to learn more about how much substorms heat up the atmosphere and how complicated and changeable this behavior is.

1. Introduction

Ionospheric conductivity plays an important role in magnetosphere-ionosphere coupling. For instance, the distributions of the ionospheric electric field and of the Pedersen conductance Σ_P determine the Joule heating of the ionosphere which has been estimated to dissipate over 50% of the total solar wind energy input to the Earth system (Østgaard et al., 2002). In addition, Joule heating is a key contributor to the power input into the thermosphere and thereby to the drag on satellites (e.g., Knipp et al., 2005). Solar irradiance and energetic particle precipitation (EPP) are both contributors to the ionospheric conductivity. The variation of the solar irradiance contribution is smooth and predictable and has a background Pedersen conductance of ~5 mho. In contrast, the EPP contribution is variable in time and space, especially during substorms (Clilverd et al., 2012). Some of the largest values of Pedersen conductance, of about 40–50 mho, have been associated with the intense auroral activity of the Westward Traveling Surge (e.g., Aikio & Kaila, 1996; Kirkwood et al., 1988). Such surges can have a scale size of several hundreds of kilometers and move

across thousands of kilometers (Craven et al., 1989). In order to calculate Joule heating during intervals of EPP, knowledge of the conductance on as fine a spatial and temporal scale as possible over the region of interest is required. In the case of a substorm, the region of interest is of continental scale.

The Pedersen conductance is difficult to routinely measure across a large area except by using global auroral satellite observations, which relies on there being an appropriate satellite in operation. Accurate specifications of Pedersen conductance may be calculated from theory using observed values of electron density (e.g., Senior et al., 2007) and model-derived values of ion-neutral and electron-neutral collision frequencies (Schunk & Nagy, 1978; Schunk & Walker, 1973). Observations of electron density from incoherent scatter radar (ISR) data sets such as those of the European Incoherent Scatter Scientific Association (EISCAT) and the Poker Flat ISR have been used to derive Pedersen conductivities in this way (e.g., Aikio & Kaila, 1996; Kaeppler et al., 2015; Kirkwood et al., 1988; Lester et al., 1996; Senior et al., 2008). The width of an ISR beam is typically ~1°, which corresponds to a horizontal distance of a few kilometers or less in the E region of the ionosphere. This should be contrasted to the spatial size associated with substorms. The size is variable (e.g., Murphy et al., 2011; Uritsky et al., 2002), but a mode analysis of 1 month of SuperMAG ground-based magnetometer data indicates the extent of the DP1 system to be ~9 hr magnetic local time (MLT) and ~2.5° latitude (Figure 6 in Shore et al., 2017) which corresponds to ~6,000 km by ~300 km, at auroral latitudes. Clearly, an ISR's limited field of view cannot be used to estimate Σ_P over such large spatial extents, leading to the compromise in the calculation of energy deposition rates (e.g., Rae et al., 2007) of using model conductances (e.g., Bilitza, 1990; Wallis & Budzinski, 1981). It is possible to extrapolate to these larger scales by combining electric field measurements with an inversion of magnetogram data, for instance, by using the Kamide-Richmond-Matsushita (KRM) technique (Kamide et al., 1981). However, both large-scale empirical models of Σ_P and values calculated through the KRM technique provide unrealistically smoothed values and thus have a limited ability to capture inhomogeneities in Σ_P of less than a few hundred kilometers in size.

To overcome such limitations, Kosch et al. (1998) related localized ISR conductances to height-integrated auroral intensities, I, measured by a ground-based television camera fitted with an interference filter at 557.7 nm. It was proposed that this relationship could allow the conductance to be inferred over the much wider fields of view of any available cameras. The various measurement methods are thus able to examine Pedersen conductances at different scale sizes: ISRs at the 1–10-km scale and the KRM technique, satellites, and empirical models at scales larger than hundreds of kilometers. The all-sky imager (ASI) technique proposed by Kosch et al. can examine the system at one location at the intermediate scale size of tens to hundreds of kilometers, which is valuable in itself, and in addition has the potential to provide such conductance values at multiple locations simultaneously. Although the estimate provided by an ASI may have its limitations, unlike empirical model values, the ASI estimate would not be a time-averaged value. In addition, unlike satellites, there are always cameras in operation, and cameras are significantly more numerous than the handful of ISRs around the world.

With these benefits in mind, it is the purpose of this paper to ask how well Pedersen conductance can be estimated from white-light all-sky cameras. We derive the relationship between Σ_P and I for the white-light ASIs of the Time History of Events and Macroscale Interactions during Substorms (THEMIS) network. These ASIs form a network over the whole North American continent and so potentially offer the multicamera exploitation proposed by Kosch et al. Due to an ASI cadence of 3 s and near-zenith spatial resolutions up to 1 km (Mende et al., 2008), the THEMIS network is potentially capable of both capturing some of the smaller-scale detail in conductance that occurs in dynamic features and also of providing the larger, substorm-scale context due to the deployment of 26 ASI locations covering 8–12 hr of MLT at auroral latitudes. In section 2, we relate the Pedersen conductance to imager intensity theoretically and describe the data sets and methodology used. We present our results in section 3. A discussion of the results is presented in section 4, and our main conclusions in section 5.

2. Data Sets and Methodology

2.1. Relating Conductance to Ground-Based Imager Intensity

For the nighttime intervals that they examined, Kosch et al. (1998) made the approximations that auroral optical intensity is proportional to ion production rate and that electron production is approximately

equal to the electron loss. Kosch et al. argued that this would mean that the conductance is approximately proportional to the square root of the height-integrated intensity. If further assumptions are made, such a relationship can be derived along the following lines. The intensity in a given imager pixel is the height-integrated emission in the atmospheric column at that horizontal location. If we assume that the auroral intensity i at a given height h is proportional to the production q of electrons (and ions) at that height, then

$$i(h) = \gamma q(h), \tag{1}$$

where γ is the constant of proportionality. This is based on the argument that any exchange of charge to release an electron causes an excitation of the atom or molecule involved that also releases a photon or photons. Then the height-integrated intensity is

$$I = \int_{h_0}^{h_1} i(h)\ \mathrm{d}h = \gamma \int_{h_0}^{h_1} q(h)\ \mathrm{d}h. \tag{2}$$

Assuming a steady-state incompressible (or static) ionosphere in which electron loss L is by dissociative recombination, then

$$q(h) = L(h) = \alpha N_e^2(h), \tag{3}$$

where N_e is the electron number density and the recombination rate is α. Substituting equation (3) in equation (2) gives

$$I = \alpha\gamma \int_{h_0}^{h_1} N_e^2(h)\ \mathrm{d}h. \tag{4}$$

The integrals in equations (2) and (4) assume that γ and α are independent of height. It is well established that the Pedersen conductivity σ_P is related to the electron density by

$$\sigma_P(h) = N_e(h)\, e\, \mu_P(h) \tag{5}$$

(e.g., Davies & Lester, 1999), where e is electric charge. The mobility μ_P varies with height because of the changes in the particle collision frequencies due to the variation in the densities of neutral species with height and also because of gyrofrequency changes due to the variation of the magnetic field with height. So the height-integrated conductivity is

$$\sum_p = \int_{h_0}^{h_1} \sigma_p(h)\mathrm{d}h = e \int_{h_0}^{h_1} N_e(h)\mu_p(h)\ \mathrm{d}h. \tag{6}$$

If we assume that the electron density maintains a given shape $f(h)$ to its altitudinal profile and that only the amplitude N_{e0} changes with time, that is,

$$N_e(h) = N_{e0} f(h), \tag{7}$$

then we can express equation (6) as

$$\sum_p = e\ N_{e0} \int_{h_0}^{h_1} f(h)\ \mu_p(h)\ \mathrm{d}h, \tag{8}$$

and equation (4) as

$$I = \alpha\gamma N_{e0}^2 \int_{h_0}^{h_1} f^2(h)\ \mathrm{d}h. \tag{9}$$

By combining equations (8) and (9),

$$I = \frac{\alpha\gamma}{e^2} \sum_p^2 \left(\frac{\int_{h_0}^{h_1} f^2(h)\mathrm{d}h}{\left[\int_{h_0}^{h_1} f(h)\mu_p(h)\mathrm{d}h\right]^2} \right). \tag{10}$$

Thus, the extent to which the emission intensity I is simply proportional to the square of the Pedersen conductance Σ_P depends on the following assumptions or approximations:

A1. The auroral intensity is proportional to the production of electrons (and ions),
A2. A steady state incompressible (or static) ionosphere,
A3. Electron loss is by dissociative recombination,
A4. The constants of proportionality γ (equation (1)) and α (equation (3)) are independent of height, and
A5. The electron density maintains a given shape $f(h)$ to its altitudinal profile and only its amplitude changes with time.

If we make these assumptions, then the height integrals relating to the profiles of electron density shape f and mobility μ_P in equation (10) are invariant, and we arrive at the parabolic relationship of Kosch et al.:

$$\Sigma_P = c_1 + a_1 I^{1/2}, \tag{11}$$

where c_1 and a_1 are constants to be determined for a given imager. Thus, the conductance can be estimated from ASI intensity using equation (11) if the coefficients c_1 and a_1 can be determined from an empirical comparison of colocated conductance and intensity measurements at some location and time. To do this comparison relies on a final assumption:

A6. The experimental setup can measure and relate the quantities Σ_P and I sufficiently well.

With regard to A6, intensity I is estimated from the raw counts C recorded by the ASI's charge-coupled device, which is a nontrivial relationship that depends on a number of factors (e.g., Mende et al., 2011). If we know this relationship, then the conductance can be derived from equation (11). Alternatively, we can estimate the conductance directly from the counts:

$$\Sigma_P = c_2 + a_2 C^{1/2}. \tag{12}$$

This has the advantage of avoiding assumptions about the imager response. However, to compare with previous studies (e.g., Kosch et al., 1998) or to estimate conductances using the other THEMIS ASIs that do not have colocated conductance measurements available for calibration (i.e., to derive parameters c_2 and a_2 at these locations), we will need to use equation (11) making use of the appropriate count-to-intensity conversion factor (Appendix, Mende et al., 2011).

Kosch et al. compared EISCAT-derived Pedersen conductance with colocated intensity data from a ground-based digital ASI. Four nights of data at 2-min resolution yielded the relationship $\Sigma_P = 0.34 + 0.18\, I^{1/2}$ where I is the observed intensity in Rayleighs (R) at a measured wavelength of 557.7 nm. However, the scatter in their data suggests that additional dependences, for example, on geomagnetic activity, might be identified and parameterized. Also, it follows from equation (10) that an additional contribution to the scatter seen will arise from the limitations of assumptions A1–A6.

2.2. Specification of the Pedersen Conductance Σ_P

The Pedersen conductivity σ_P is the component of the electrical conductivity in the Earth's ionosphere that is parallel to the electric field and perpendicular to the magnetic field. σ_P peaks at approximately 110–130 km in the upper E region of the ionosphere due to the high collision rate between ions and neutrals at these altitudes. In contrast, the collision rate between electrons and neutrals is much lower. Hence, there is a resultant difference in the electric-field drift of the electrons and ions. The Pedersen conductivity is given by equation (5). The mobility μ_P is dominated by the contribution due to collisions between ions and neutrals so can be approximated by

$$\mu_P = \frac{\mathbf{1}}{B}\left(\sum_j P_j \frac{\omega_j \nu_{jn}}{\omega_j^2 + \nu_{jn}^2}\right), \tag{13}$$

where B is the geomagnetic flux density, ω_j is the gyrofrequency of ion species j, ν_{jn} is the ion-neutral collision frequency for ion species j, and P_j is the relative density of ion species j. The ion-neutral collision frequencies depend on the number densities of N_2, O_2, and O and on the average of the neutral temperature T_n, and the ion temperature T_i (Appendix in Schunk & Walker, 1973). The neutral number densities and temperature are calculated using the MSIS model (Picone et al., 2002). The ion temperature is measured by the ISR, as is the electron number density used to calculate the conductance Σ_P in equation (6).

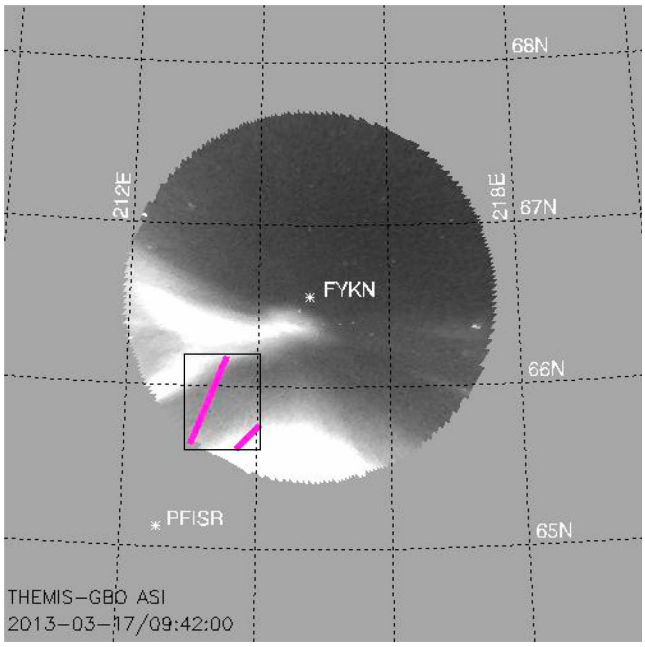

Figure 1. Location of experiment. The location of the PFISR (white asterisk) and of the beams of the 1-min PFISR data used (pink solid lines); the location of the FYKN ASI (white asterisk) and the field of view for elevation angles $\alpha \geq 48°$. The solid black box represents the latitudes and longitudes of the data used. FYKN = Fort Yukon; PFISR = Poker Flat Incoherent Scatter Radar; THEMIS = Time History of Events and Macroscale Interactions during Substorms; GBO = Ground-Based Observatory; ASI = all-sky imager.

2.3. Poker Flat ISR (PFISR)

We use data from the Poker Flat ISR (PFISR) located at the Poker Flat Research Range northeast of Fairbanks, Alaska, at 65.13°N, 212.53°E (see Figure 1; Kelly & Heinselman, 2009; Nicolls et al., 2007). PFISR is an Advanced Modular ISR colocated with the equatorward edge of the nightside auroral oval. PFISR has been used in conjunction with THEMIS Ground-Based Observatory data to study ionospheric electrodynamics, for instance, during the substorm expansion phase (e.g., Zou et al., 2009). PFISR can provide accurate local values of Pedersen conductivity values, as outlined in section 2.2.

In this study, we use PFISR data collected during two "PFISR Ion-Neutral Observations in the Thermosphere (PINOT)" campaigns conducted in November 2012 and March 2013. The data used in this study were collected during the "PINOT_Nighttime31" experiment (supporting information Figure S1), which was an 11-beam mode using single frequency 480-μs fractional lag Alternating Code (AC) pulses (Huuskonen et al., 1996). The AC used sixteen 30-μs bauds, oversampled at 10 μs, resulting in a range resolution of approximately 9 km. The PFISR AC data were integrated to 1-min time resolution and were fitted for altitudes ranging from 86 to 335 km. Figure 2 shows the spatial distributions of the PFISR AC data. Each 1 min of PFISR AC data comprises measurements at 38 heights. The PFISR beam directions (Figure S1) are not aligned to the magnetic field direction. An along-*B* configuration, which was used by Kosch et al., is required for highly precise studies attempting to relate height-integrated conductivity and auroral emissions. However, as discussed in section 1, the purpose of this study is to enable the exploitation of ASI data across the entire THEMIS network, without needing to know the details of the magnetic field configuration. We discuss the effect of using this configuration on our results in section 4.

The standard SRI International fitting software was applied to the AC data for this study. The SRI fitter utilizes an ion photochemistry model called "flipchem" based on the Field Line Interhemispheric Plasma ion composition model (Richards, 2011), to estimate the ionospheric ion composition. Using flipchem, the ISR data are fitted using ion composition profiles for five dominant ion species in the E and F regions: O^+, $O_2{}^+$, NO^+, $N_2{}^+$, and N^+. Since the ISR-fitted parameters, especially T_e and T_i, depend on ion composition (e.g., Zettergren et al., 2010; Zou et al., 2017), using flipchem provides a realistic first-order estimate of the ion composition.

2.4. THEMIS Ground-Based Observatory Network

The THEMIS Ground-Based Observatories are an array consisting of over 20 ASIs and more than 30 magnetometers which span the North American continent (Mende et al., 2008). Each observatory ASI is a white-light imager recording data at a cadence of 3 s. Modeling for the THEMIS cameras shows that the imager primarily responds to electron precipitation energies greater than 3 keV (Mende et al., 2008) and thus responds primarily to the 557.7 nm green auroral emission line. We hence assume that the peak of the emission height is at about 110 km altitude.

Pedersen conductivity varies by a factor of about two in response to an order of magnitude variation in the precipitating energy (Vickrey et al., 1981) and is generally associated with precipitation in the energy range 2–10 keV (Senior et al., 2007). The variability in the energy of the precipitation will be associated with variability in the ASI response function.

The thumbnail summaries of THEMIS ASI data were used to select intervals of ASI data during the PINOT Campaign near Fort Yukon (FYKN). The FYKN ASI is located at 66.560°N, 214.786°E (Figure 1). We use four nights with a clear view of the sky, low moonlight pollution, and readily available (not special mode) PFISR data (Table 1). We discarded data outside of Astronomical Twilight which is defined in Text S1.

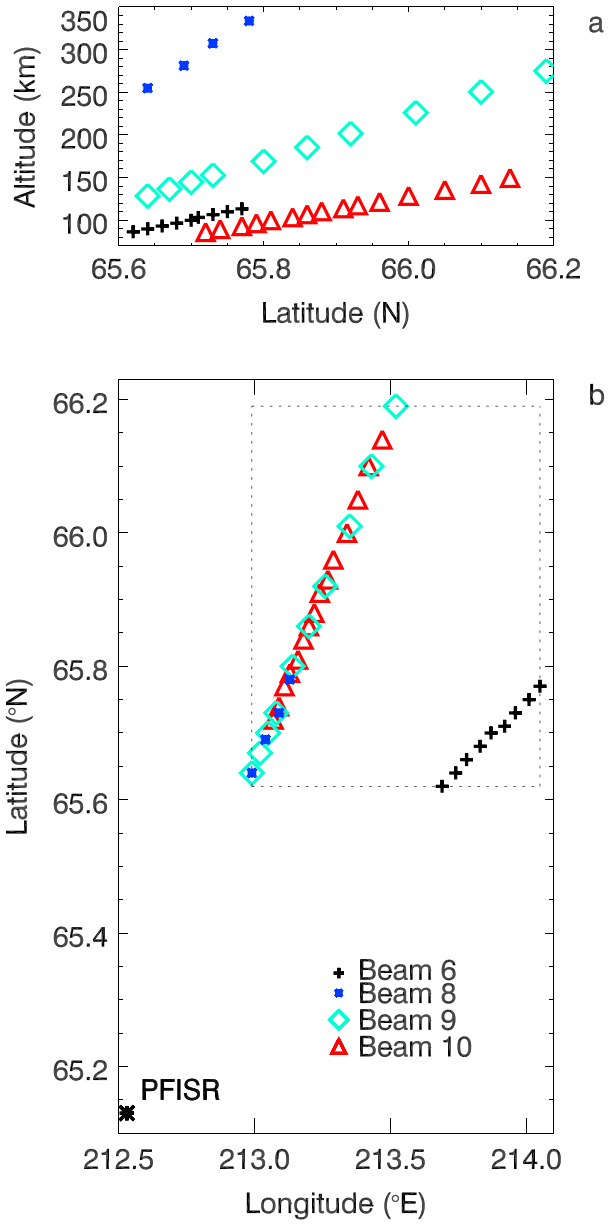

Figure 2. Spatial distribution of PFISR beams. (a) The latitude-altitude dependence of the PFISR data. The symbols identify data from different beams (legend in Figure 2b); (b) the latitude-longitude dependence. The dotted box marks the latitude-longitude range of the data used (see also Figure 1). PFISR = Poker Flat Incoherent Scatter Radar.

These intervals have a range of geomagnetic activities with values of the planetary index K_P from 0 to 6 (Bartels, 1949). We used the Space Physics Environment Data Analysis Software (SPEDAS) Interactive Data Language (IDL) software to download and manipulate the THEMIS ASI data set.

Using a star field, each pixel in the ASI is assigned a latitude and longitude range as projected to 110 km altitude. From this, a virtual image of the auroral measurements can be constructed at this assumed emission altitude, which we can then compare to the ISR measurements. However, this means that the latitude and longitude of a pixel of ASI data are most accurately known close to the ASI zenith, that is, at an elevation angle $\delta \sim 90°$ above the horizon (Mende et al., 2008). For such high elevation angles, the horizontal extent of the ionosphere being imaged is relatively small compared to that for a low angle, and the pixel can in principle capture the emissions that occur in the vertical column above. In contrast, an ASI pixel that receives light from just above the horizon is imaging a much greater horizontal extent and is not capturing all the light in the corresponding column. Consequently, it is recommended that for some studies, the data used are restricted to relatively high elevation angles, for example, $\delta \geq 70°$. For this study, however, we relax that criterion. To test and refine the relationship between colocated conductance and optical intensity, we use the ISR data down to the lowest available altitudes at about 85 km and an elevation angle criterion of $\delta \geq 48°$. In practice, we must compare the ASI count and the Pedersen conductance within a volume V (Figure 2). The effect of the experimental setup is discussed further in section 4.

2.5. Testing the Kosch et al. (1998) Relationship

For each chosen interval (Table 1), we calculate the mean Pedersen conductance $\Sigma_P(t)$ within a volume V, at 1-min resolution. We use a cuboid volume in height, latitude, and longitude where there are both PFISR data for the whole height range and ASI data with an elevation angle $\delta \geq 48°$. The volume V is defined by 86–336 km altitude and the approximately 60 km by 50 km geographic region 65.62–66.19°N, 212.99–214.05°E (Figure 2). The conductance is estimated from the height integral of the available conductivity values $\sigma_P\ (\lambda, \phi, h, t)$ due to ion-neutral collisions for each PFISR data point at latitude λ, longitude ϕ, height h, and time t. We can express the conductivity as $\sigma_P\ (\lambda, \phi, h, \mathrm{n}\ \Delta t)$ where n labels each minute.

The frequency spectra of the ISR signal provide information about the electron density, plasma velocity, ion mass, and the ion and electron temperatures. Such information is estimated from the theoretical spectrum by finding the temperatures and velocity that most closely yield the measured spectrum. We do not find any instances where the electron or ion temperatures are negative. There are a small number of occasions when $N_e < 0$ and these data are discarded. Unphysical negative values can arise as a result of a poor fit of the data to the theoretical spectrum. This occurs when a noisy autocorrelation function results in convergence on a "bad" value, with associated large errors in the fit. We also discard one occasion when $N_e > 10^{13}$ m^{-3} which may be due to backscatter from space debris or satellites. For the volume V, we calculate a conductance from the conductivity-height "profile" formed by the conductivities collected at different heights along the PFISR beams and compare with the mean optical intensity associated with that volume. We are making the assumption that there is spatial homogeneity in both the conductance and the height-integrated optical intensity associated with the volume V which, of course, will not always be the case.

Table 1
The Date and UT Range of the Intervals of Data Used in This Study

Date	UT range	K_P	ASI count	Error (mho)	Error (%)
8 Nov 2012	6–15	0 and 1	<1,000	2.7	33
7 Nov 2012	9–15	1 and 2	<2,000	1.3	51
16 Mar 2013	7–10	2 and 3	<3,000	2.6	17
17 Mar 2013	7–10	5 and 6	<12,000	5.7	62

Note. The associated values of K_P, the maximum ASI count, the absolute and the relative differences between the ASI specification of conductance, and the Poker Flat Incoherent Scatter Radar-derived values of conductance averaged over 10 min. UT = Universal Time; ASI = all-sky imager.

In order to capture the peak of the Pedersen conductance, we ensure that the range 90–185 km is particularly well represented by data. Hence, for each 1 min of data, we only proceed when the associated conductivity data meet the following criteria: ≥30 values (~75%) for the whole height range (~86–336 km); ≥20 values (~75% of the profile data) between ~90 and 185 km; and at least one value at (i) 86 km, (ii) ~281–334 km, (iii) ~151 km, (iv) ~169–185 km, (v) 202 km, and (vi) 226 km. For each 1 min of data, we only derive a conductance value when there is a sufficiently well-defined conductivity-height "profile" to do so. The altitude profiles of the mean conductivity derived in this way are shown in Figure 3, for each of the intervals used in our study, and the corresponding electron density profiles are shown in Figure S2. A comparison of the mean conductivity and electron density profiles for the intervals used are shown in Figure S3. For each interval, Figure 3 shows that the conductivity falls to roughly 10% of the peak value at ~90 and ~185 km. If the data for a given 1 min meet the quality criteria, then linear interpolation (using IDL's "interpol" routine) is used to fill in any missing conductivity values, and the conductivity is integrated in height to produce the 1-min conductance values, $\Sigma_P(\lambda, \varphi, n\Delta t)$. The use of the quality criteria means that there are conductance values missing for some times. We did not fill these values using interpolation but instead discarded those times from the study. The method is a balance between obtaining a reasonable measure of conductance, on scale of tens of kilometers between 86 and 300 km, and retaining a large enough sample of 1-min data to gain a statistical picture of the relationship between conductance and image intensity.

For each interval in Table 1, we also obtain the mean ASI count associated with the volume V (Figure 2) over 1 min, $C_v(n)$. The time stamp for the 1-min AC data occurs at the middle of the time window in which the AC data were collected. As discussed in section 1, using this cuboid rather than a narrow magnetic-field-aligned column is a source of variability or error in testing the relationship of ASI counts to conductance which we shall examine. This is in part because the conductance may not be representative of the whole geographical area and time but rather reflect the variability picked up by the narrow ISR scans, whereas we find a mean value of the counts over the whole geographical area.

3. Results

3.1. Using Data From All Intervals

Following the quality checks discussed above, the studied intervals (Table 1) yield 515 pairs of conductance-count data points. During intervals of quiet geomagnetic activity, the conductance values are between ~1 and 5 mho, as expected (e.g., Aikio & Selkälä, 2009; Lester et al., 1996). We find that 38% of the values are below 5 mho, 70% of the values are below 10 mho, and 94% are below 20 mho. The highest values of conductances occur during several time sequences on 17 March 2013, rather than as isolated values (see Figure 8 below), and correspond to intervals of high ASI count, indicating that these high conductances are not spurious data points. The highest conductances (some about 30 mho and one at 64 mho) are associated with intense auroral activity, as verified by examining the THEMIS ASI thumbnails for these times. For example, http://themis.ssl.berkeley.edu/gbo/display.py?date=2013.03.17&view_type=summary&id=FYKN.2013.03.17.07.00 accesses the images for around 07:00 UT on 17 March 2013.

Figure 4 shows a scatter plot of the Pedersen conductance against the associated mean ASI count in the volume V. We see nonzero counts when the conductance is close to zero. This indicates the presence of a background count due to artificial light pollution and the dark count. In order to quantify the relationship of conductance to count given by equation (12), we remove this background intensity, $b_2 = 2{,}866$ counts, beforehand. That is, we substitute

$$C = C_V - b_2. \tag{14}$$

We use the IDL "curvefit" routine to find the values of the parameters a_2 and c_2. The routine uses a gradient-expansion algorithm to compute a nonlinear least squares fit to a user-supplied function $F(C)$. We use the

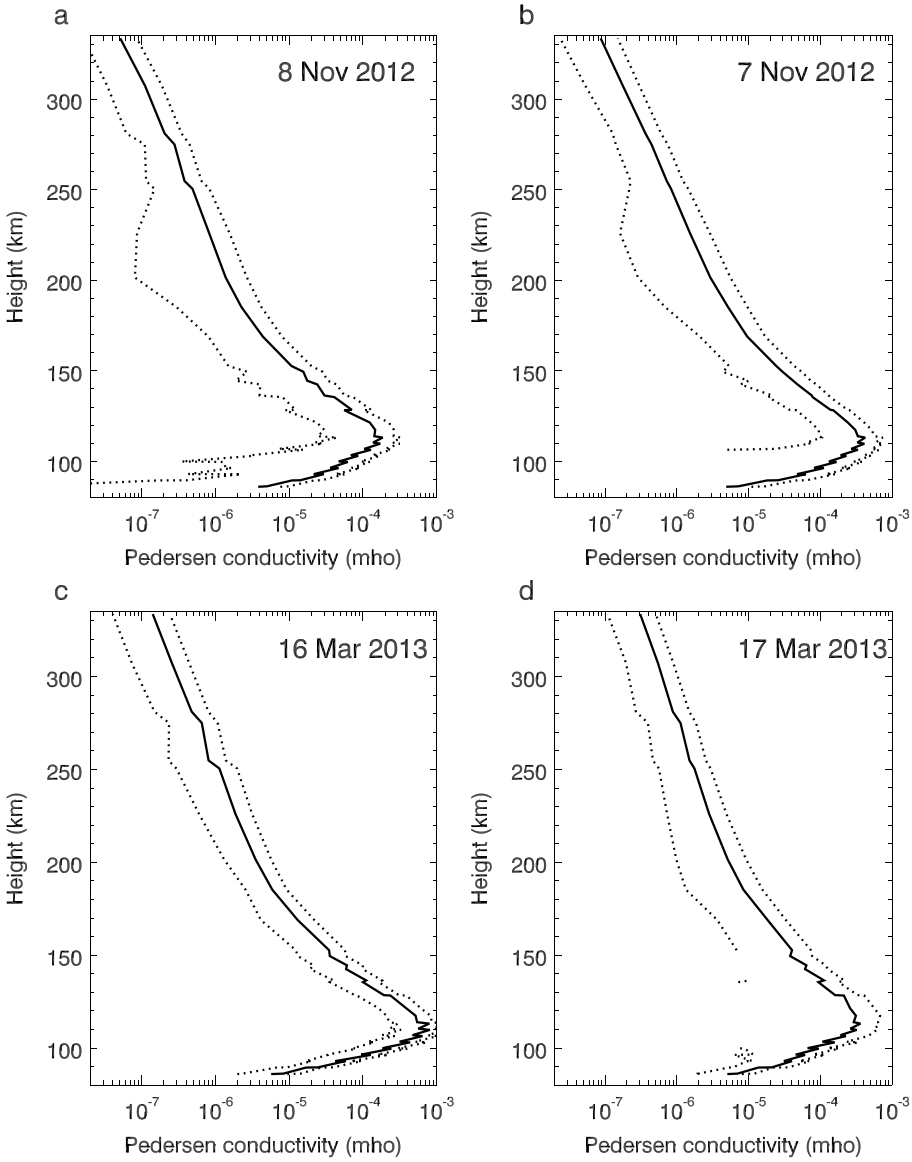

Figure 3. Pedersen conductivity height profiles. (a–d) The mean Pedersen conductivity-height profile (solid black) for the four intervals listed in Table 1. Dotted lines lie one standard deviation away from the mean value. Figure S3a shows the mean profiles in (a)–(d) superimposed.

standard deviation (SD) in the mean count for each 1 min (Figure S4) to provide a measure of the instrumental (Gaussian) weighting in the routine. For b_2 = 2,866 counts, we find that the data are fitted to equation (12) by a_2 = 0.38 and c_2 = 0.01, with associated uncertainties related to the SD of the two fitting parameters a_2 and c_2.

However, since c_2~0, we can alternatively fit the data to equation (15) below with just a single free parameter a_2. In this case, taking logs of each side of equation (11) yields

$$\log\Sigma_P = \log(a_2) + 0.5\ \log(C), \tag{15}$$

and the free parameter can then be estimated by linear regression using IDL's curvefit. The result (i.e., for b_2 = 2,866 counts and c_2 = 0) is a_2 = 0.35 mho per (count)$^{1/2}$ (solid red line in Figure 4), with a SD = 0.4 mho per (count)$^{1/2}$. The χ^2 statistic is 0.01, which is significant at the 5% level. For future reference, we note by eye that most 1-min values in Figure 4 are bounded by the lines $\Sigma_P = 0.4\ a_2 C^{1/2}$ and $\Sigma_P = 2.5\ a_2 C^{1/2}$ (dashed red lines), representing a factor of 6.25 variation in the parameter a_2.

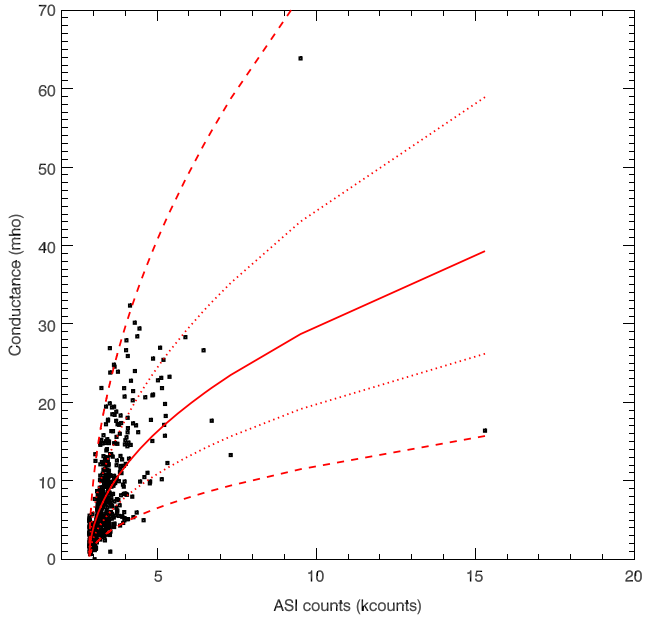

Figure 4. Dependence of Pedersen conductance on ASI count for the current study. The scatter plot shows Pedersen conductance against ASI count. The line of best fit to the function $\sum_P = a_2\, C^{1/2} + c_2$ for $C = C_v - b_2$, where $a_2 = 0.35$ mho per (count)$^{1/2}$, $b_2 = 2{,}866$ counts, and $c_2 = 0$ mho (solid red). The dotted red lines represent the standard deviation in the fitted value of a_2. The lines $\sum_P = (a_2/2.5)\, C^{1/2}$ and $\sum_P = 2.5 a_2\, C^{1/2}$ (dashed red) envelope most of the data. ASI = all-sky imager.

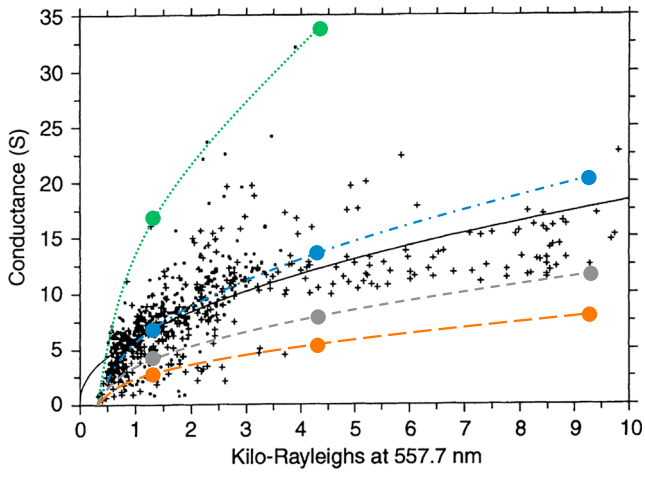

Figure 5. Kosch et al. (1998) dependence of Pedersen conductance on optical intensity. Scatter plot of Pedersen conductance in Siemens (S, equivalent to mho) against optical intensity shown by the dots ($K_P < 4$) and crosses ($K_P \geq 4$) and the line of best fit as given by Kosch et al. (black solid line); our estimate of the upper and lower envelopes of the data points of Kosch et al. for which $a_1 = 0.54$ (green dotted line) and $a_1 = 0.09$ (orange long-dashed line), respectively, and the intermediate parabola, for which $a_1 = 0.22$ (blue dot-dash line); the line of best fit (Figure 4) found by the current study $\sum_P = a_1\, I^{1/2}$ for which $a_1 = 0.12$ (gray short-dashed line). Adapted from Figure 2b of Kosch et al. (1998).

We shall now compare the conductance-count relationship for the FYKN THEMIS ASI with the results of the study of Kosch et al. The Kosch et al. results are reproduced in Figure 5 where the data are shown by the black symbols and their best fit relationship $\Sigma_P = 0.34 + 0.18\, I^{1/2}$ is shown by the black solid line. A similar fit through the data is given by the parabola $\Sigma_P = 0.22\ (I - 300)^{1/2}$ (blue dot-dash line), which we think is preferable because the conductance now goes to zero at the lower bound of their data.

By eye, we estimate that most of the data points of Kosch et al. are enveloped by $\Sigma_P = 0.54\ (I - 300)^{1/2}$ (dotted green line) and $\Sigma_P = 0.09\ (I - 300)^{1/2}$ (long dashed orange line). Thus, the upper envelope has a value of $a_1 = 0.22 \times 2.5$, and the lower envelope has a value of $a_1 = 0.22/2.5$. Hence, the data of Kosch et al. are bounded by the same multiplicative factor ($2.5 \times 2.5 = 6.25$) that bounds the data of our study.

In order to compare Kosch et al.'s conductance-intensity relationship to the conductance-count relationship that we have derived from our data shown in Figure 4, we convert the FYKN ASI counts to optical intensity using the conversion factor $f = 0.118$ counts per R of 557.7 nm given in the Appendix of Mende et al. (2011). Using the value of $a_2 = 0.35 \pm 0.4$ mho per (count)$^{1/2}$, this gives a value of $a_1 = 0.12 \pm 0.14$ mho per $R^{1/2}$ and hence a conductance-intensity equation:

$$S_p = 0.12\ (I_V - b_1)^{1/2}, \tag{16}$$

where $b_1 = C_v/f = 24{,}288\ R$ for the FYKN ASI. Thus, our offset b_1 is much larger than that of the imager used by Kosch et al., reflecting the different site environments. More importantly, our value of $a_1 = 0.12$ mho per $R^{1/2}$ is smaller than either the corresponding value of $a_1 = 0.18$ mho per $R^{1/2}$ found by Kosch et al. (1998) or the value of $a_1 = 0.22$ mho per $R^{1/2}$ which is our fit to the Kosch et al. data but not statistically different. For comparison, we show equation (16) in Figure 5 by the gray dashed line where we have used the Kosch et al. value of $b_1 = 300\ R$.

3.2. Case Studies

The scatter in the results of Kosch et al. (Figure 5) and in our corresponding results (Figure 4) may be due to further dependences, for instance, on levels of geomagnetic activity or due to limitations in the assumptions made (A1–A5) in deriving equation (11) or in the experimental setup. In addition, it is not possible to see the detail of the data points in Figure 4, even if we use logarithmic scales (not shown). Therefore, in Text S2 and via Figure S5, we give background information about the K_P indices and the SuperMAG Auroral Electrojet Lower index (Gjerloev, 2012; Newell & Gjerloev, 2011). We also describe the conductance-count relationship for the individual days (Figures S6–S9). Text S2 describes short intervals (up to 30 min) of variability in the PFISR values of conductance accompanied by low variation in ASI count. If an auroral optical feature crosses through the volume examined, the volume-mean count C_V can be reasonably constant for the time it takes to pass through the volume. The conductance, however, is only observed to rise or fall when the structure intersects with the radar beams, for example, 13:30–14:00 Universal Time (UT), 14:00–14:30 UT, and 14:30–15:00 UT on 8 November 2012.

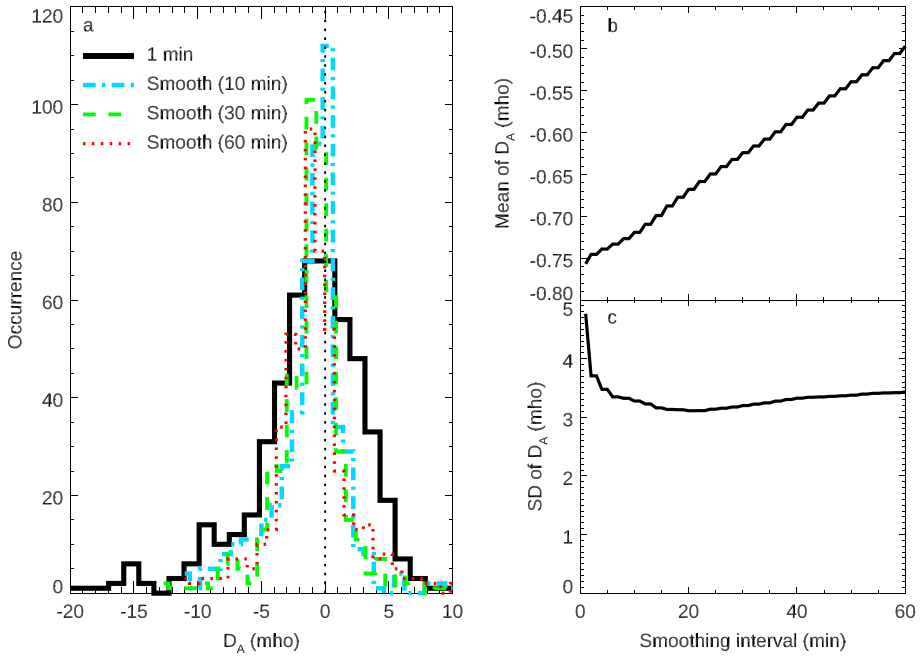

Figure 6. Effect of temporal smoothing on absolute difference between all-sky imager- and Poker Flat Incoherent Scatter Radar-derived Pedersen conductances. (a) The histogram (black) of the absolute difference $D_A = S_p - \Sigma_P$ for the 1-min data of Figure 4 (black squares). Histograms of D_A for Poker Flat Incoherent Scatter Radar data smoothed over 10 min (blue dot-dash), 30 min (green dash), and 60 min (red dotted); (b) the mean of D_A as a function of smoothing interval; (c) the standard deviation (SD) of D_A as a function of smoothing interval.

This accounts for some of the scatter observed in Figure 4. The degree of variability of the optical data is discussed further in Text S3.

We also see strong evidence of the parabolic nature of the relationship between conductance and ASI count in some intervals of the data set, for example, 07:00–10:00 UT on 17 March 2013 shown in Figure S9. There is a lower limit to the background count seen in Figures 4 and S6 to S9, which is likely to be dominated by artificial light pollution. Some of the parabolic forms also appear to have a nonzero conductance offset of ~5 mho. We propose that the parabolic behavior in the conductance-count relationship is related to additional EPP and that the background conductance is related to other sources of conductivity such as transport and airglow.

3.3. Time-Averaged Behavior

Some of the scatter in Figure 4 is due to auroral optical features advecting through the volume and will be reduced by appropriate time averaging of the PFISR conductance data. Therefore, in this subsection, we calculate the absolute difference between the ASI specification of conductance S_p and the PFISR-derived values, that is, $D_A = S_p - \Sigma_P$ for different intervals of time smoothing of the 1-min Σ_P.

Figure 6a shows the distribution of D_A for the 1-min values of S_p and Σ_P presented in section 3.1 and plotted in Figure 4 (black squares). The other histograms in Figure 6a show the effect of smoothing the 1-min Σ_P data over different time periods between 10 min and 1 hr. Increasing the length of the smoothing interval from 1 to 10 min slightly decreases the size of the mean value of D_A from −0.76 to −0.72 mho (Figure 6b). The SD of D_A decreases as the smoothing interval is increased from 1 to 10 min from 4.8 to 3.3 mho (Figure 6c). Further increasing the interval size from 20 to 60 min results in a small degree of variation in the SD of D_A.

We also examine the relative difference between the ASI specification of conductance and the PFISR-derived values of conductance Σ_P, that is, $D_R = (S_p - \Sigma_P) / \Sigma_P$. Figure 7a shows the effect of smoothing the 1-min Σ_P data on the distribution of D_R. Increasing the length of the smoothing interval from 1 to 10 min decreases the size of the mean value of D_R from 21% to 0% (Figure 7b). The SD of D_R decreases as the smoothing interval is

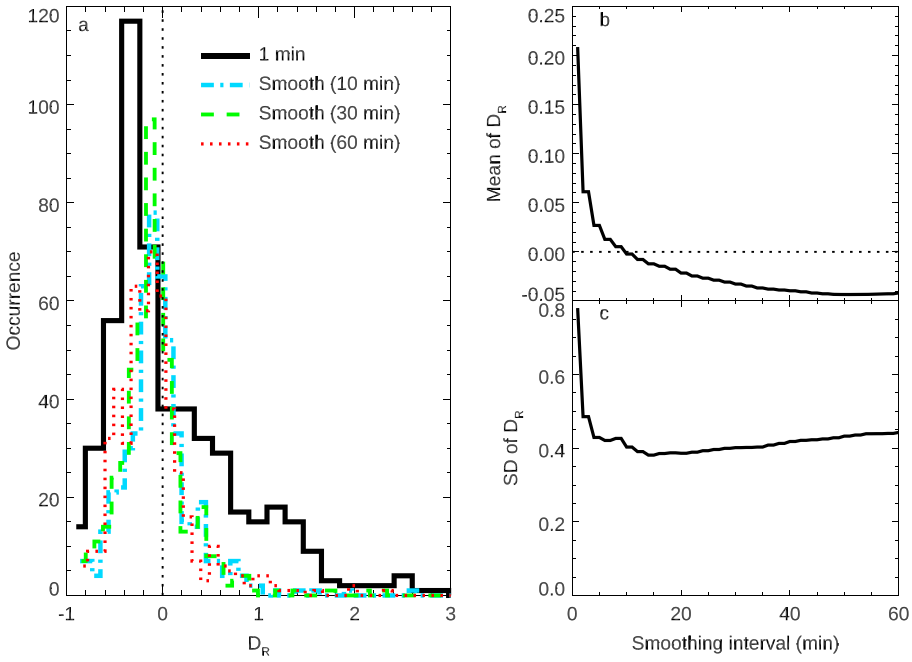

Figure 7. Effect of temporal smoothing on relative difference between all-sky imager- and Poker Flat Incoherent Scatter Radar-derived Pedersen conductances. As for Figure 6 but calculated for the relative difference $D_R = (S_P - \Sigma_P) / \Sigma_P$. SD = standard deviation.

increased from 1 to 10 min from 78% to 40% (Figure 7c). Further increasing the interval size from 20 to 60 min decreases the mean asymptotically to −0.05 and slightly increases the SD of D_R. The nonzero asymptotic value may be due to a small offset in the conductance. If D_A and D_R are calculated for the individual nights (Table 1), then we observe similar trends in the mean and SD of the values as a function of smoothing interval (not shown). The values of the absolute and relative errors are given in Table 1 for the individual events, as well as K_P and the maximum ASI count. There is no clear trend in the error with either K_P or ASI count, though the maximum error is associated with the highest values of emission intensity (and K_P).

Since using a smoothing interval of 10 min significantly decreases the size of the mean and SD values of D_R, we now compare the Pedersen conductance values estimated from ASI data (black squares, Figure 8) with the 10-min-averaged PFISR Pedersen conductance values (red diamonds, Figure 8) in the time domain. In general, we find very good agreement between the ASI and PFISR-derived measurements on a 10-min timescale. Although we may not have removed an offset in the conductance, as evidenced by the asymptotic value of −0.05 in Figure 7b, nevertheless, for the data set we are using, a smoothing interval of 10 min achieves the minimum in D_R and so is the most appropriate for a comparison with the ASI data. The shape of the ASI specification of Pedersen conductance variation sometimes differs noticeably to that of the smoothed PFISR values of Σ_P. Identifying the exact causes of the offsets is beyond the scope of this study, but we note that the ASI value may fall below the PFISR value if optical emissions are not dominated by the green line, but especially if cloud reduces the ASI measurement of optical intensity. And, on the other hand, if optical emissions of significant amplitude never become colocated with the ISR radar, then the PFISR value can instead fall below the ASI value. The comparison of the Pedersen conductance values estimated from ASI data with the 1-min PFISR Pedersen conductance values (blue crosses, Figure 8) is much poorer, as expected from the results of Figures 6 and 7.

4. Discussion

In this section, we summarize the results and conclusions obtained so far and assess their validity and importance. The PFISR can be and is often used to perform highly detailed and sophisticated studies, but here we have used both the PFISR and the ASI data in a comparatively large-scale and approximate fashion; for

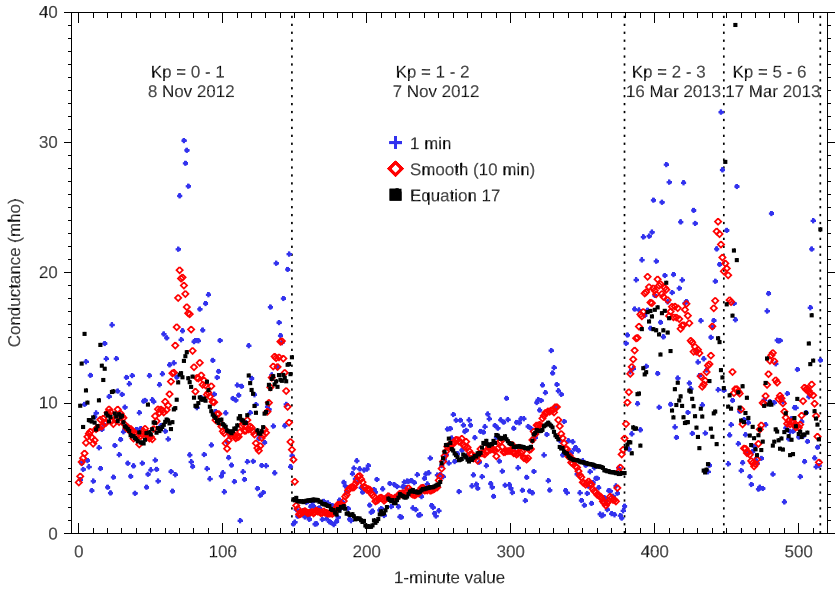

Figure 8. Time-domain comparison of the all-sky imager-derived Pedersen conductance with the PFISR-derived value. For each of the four intervals examined (Table 1), we plot the 1-min PFISR values of Σ_P (blue crosses), the 1-min PFISR values smoothed over 10 min (red diamonds), and the 1-min values of S_P (equation (16)) derived from all-sky imager data (black squares). The conductance is only plotted up to a value of 40 mho for clarity (a single 1-min data point exceeds this at ~64 mho). PFISR = Poker Flat Incoherent Scatter Radar.

instance, we have made use of nonmagnetic-field-aligned radar data and of camera data that is off-zenith. In section 4.1, we note the strong similarity of our results with the study of Kosch et al. (1998), which did use magnetic-field-aligned radar data. We argue that this strongly helps to validate our methodology, including the use of the assumptions made in section 2.1. In section 4.2, we revisit those assumptions in light of our results.

4.1. Our Key Results and Comparison to Kosch et al. (1998)

In this paper, we investigate the dependence of Pedersen conductance Σ_P on auroral intensity I using white-light data from the Fort Yulon THEMIS ASI and Poker Flat ISR data, together with modeled ionospheric collisional frequencies. We fit the data from four nights with a range of values of K_P to the curve $\Sigma_p = 0.12\, I^{1/2}$, where I is the observed intensity in R with the background intensity removed, and we find that most Σ_p data are bounded within a factor of ~6 (Figure 4). We show that a THEMIS white-light ASI can estimate Pedersen conductance with an uncertainty of 3 mho or 40% on scales of 1–10 min and ~100 km^2. ISR is excellent at determining localized values of conductance. If we can place confidence in this derived relationship, the THEMIS ASI network presents an opportunity to usefully assist in the identification of regions of large and low conductance. This would be a significant aid in exploring Pedersen conductances in the context of substorms.

One of the key findings of our study is that there is a strong similarity between our results and those of Kosch et al. who examine optical emissions at 557.7 nm, also for four nights with a range of K_P values using EISCAT ISR data. The Kosch et al. study uses a magnetic-field-aligned ISR beam, 2-min resolution data, and a 10 km by 10 km optical cell, whereas our study uses nonmagnetic-field-aligned results with 1-min resolution, from a 60 km by 50 km region, where data from different altitudes come from different horizontal locations. Kosch et al. fit the data to the curve $\Sigma_P = 0.34 + 0.18\, I^{1/2}$ (Figure 5). Their data show a similar level of scatter to our results, with the majority of the data also bounded within a factor of ~6 (Figure 5). Our results not only confirm the parabolic relationship derived by Kosch et al. but also strongly suggest that only some of the scatter in our results (Figure 4) is due to the differences between the two experimental setups, such as the size of the volume examined, the relationship of the ISR beam to the magnetic field direction, and the wavelength of the optical measurements. In summary, the THEMIS cameras can provide a constraint on the

Pedersen conductance to within 40% on a scale of 10–100 km on a timescale of 10 min, regardless of the knowledge of the relationship of the data to magnetic field direction.

4.2. The Assumptions

The discussion in section 4.1 shows that our experimental setup is adequate and validates assumption A6. The similarity of the ASI-derived conductance S_p to the results of Kosch et al. strongly suggests that equation (16) may even hold to the finer spatial and temporal scales which they examined. In addition, we have a possible explanation for the similarity of the ASI-derived conductance S_p to the 10-min-averaged PFISR conductance in terms of our experimental setup. That is, if an auroral optical feature crosses through the volume examined, the volume-mean count can be fairly constant for the time it takes to pass through the volume, and the conductance is only observed to rise or fall when the structure intersects with the radar beams.

In this subsection, we revisit our assumptions in light of the results. Theoretically, under assumptions A1–A5 listed in section 2.1, we find that Σ_P is proportional to $I^{1/2}$. Kosch et al. argue that the assumption that the auroral intensity is proportional to the production of electrons (assumption A1) should hold to first order, since for a particular precipitation rate, particles of approximately a single energy will produce an approximately constant rate of auroral photons. The assumption of a static ionosphere (assumption A2), however, is a gross simplification that will certainly not always hold. The fact that the data are bounded by a variation in the constant of proportionality of the parabola of a factor ~6 (Figures 4 and 5), however, means that our set of assumptions is actually a pragmatic choice for the design and purposes of this study.

Below ~160 km, loss of electrons is predominantly via dissociative recombination (Hargreaves, 1979). The Pedersen conductivity generally peaks in the range 100–130 km (Senior et al., 2007) as is confirmed by Figure 3, so we assume that dissociative recombination dominates loss processes. If so, we expect a dependence of Pedersen conductance on $I^{1/2}$ or $C^{1/2}$ (equations (11) and (12)). The scatter of all the data is convincingly fitted and bounded by curves of the form $a\ C^{1/2}$ (Figure 4), and some individual 1-hr intervals (Text S2) indicate a dependence of Σ_P on $C^{1/2}$ as shown by the parabolic forms in Figures S6, S7, and S9. Therefore, an assumption that loss of electrons is via dissociative recombination (assumption A3) works well.

We have assumed that the constants of proportionality in equations (1) and (3) are independent of height (assumption A4) in the derivation of equation (11). The altitude to which precipitation penetrates is energy dependent. The energy dependence of precipitation will therefore contribute to some of the scatter observed in Figures 4 and 5. We have also assumed that the electron density maintains a given shape to its altitudinal profile (assumption A5). The mean electron density profiles for our intervals are shown in Figures S2 and S3b. The variability indicated in the figures shows that the shape of the electron density altitudinal profile ($f(h)$ in equation (7)) is time varying. Factors containing the function $f(h)$ in equation (10) will also be time-varying, meaning that assumption A5 does not always hold. It is likely that the temporal and altitudinal variation in the factors that multiply Σ_P^2 in equation (10) are important to the scatter of Figure 4, because the data set includes clearly visible curves which correspond to a $C^{1/2}$ form but with different shapes at different times (e.g., Figures S7b and S9). Therefore, we propose that the breakdown of assumptions A4 and A5 is key to determining the upper and lower bounds of the scatter in Figure 4.

5. Conclusions

In conclusion, using large-scale (~100 km by 100 km) and 1-min-averaged ASI data colocated with measurements of ionospheric conductance, we find that:

1. A THEMIS white-light ASI can produce a good proxy for ISR Pedersen conductance with an uncertainty of 3 mho or 40% on spatial scales of ~100 km^2 if the ISR data are averaged over ~10 min.
2. We can relate the Pedersen conductance to the white-light optical intensity with a single parabolic relationship across a wide range of geomagnetic indices ($K_P = 0$–6). The relationship is $\Sigma_p = 0.12\ I^{1/2}$ where I is the observed intensity in Rayleighs with the background intensity removed.
3. Most Σ_p data are bounded by a factor of 6 to this simple relationship, despite the use of large-scale means of data that are not aligned to the magnetic field.

4. There are strong similarities between our results and those of Kosch et al. (1998) who used single-wavelength, magnetic-field-aligned data, indicating that the relationship presented in this paper is robust and can be used to exploit THEMIS ASI data.

Joule heating during a geomagnetic substorm is a critical component of its energy budget and can be estimated to account for over 50% of the total solar wind energy input to the earth system within one substorm (Østgaard et al., 2002). However, in order to make quantitative measurements of Joule heating, it is essential to understand the contributions across the very large range of latitudes and MLTs that substorms expand into. In this paper, we have demonstrated that the dense array of white-light auroral cameras of the THEMIS ASI network could usefully assist in the identification of regions of high and low Pedersen conductance on a scale of 10–100 km at multiple imager locations, on a timescale of 10 min.

As mentioned in section 4.2, the similarity of the ASI-derived conductance to the 10-min-averaged PFISR conductance and to the results of Kosch et al. suggests that our ASI proxy for conductance actually holds to finer scales. This method is therefore of great value given the number of ASI networks available. The existence of the THEMIS ASI archive of data, in particular, and the limited options for observing Pedersen conductance on the spatial scale of a substorm mean that this result could improve conductance estimates of features such as the Westward Traveling Surge and substorm-related Joule heating on continental scales.

Acknowledgments
We thank Andrew Kavanagh of the British Antarctic Survey (BAS) for useful discussions. A significant part of this work was completed while M. M. L. was a visitor to the BAS, UK. M. M. L. gratefully acknowledges financial support by MSSL (no grant number). PFISR operation, maintenance, and data distribution is supported by NSF Cooperative Agreement AGS-1133009 to SRI International, and all PFISR data are available in the Madrigal Database (http://isr.sri.com/madrigal) and from the Principal Investigator for the specific experiment. We gratefully acknowledge generous PFISR data support by Ashton Reimer (SRI International). We acknowledge NASA contract NAS5-02099 and V. Angelopoulos for use of data from the THEMIS Mission and specifically S. Mende and E. Donovan for use of the ASI data. We thank the CSA for logistical support in fielding and data retrieval from the GBO stations and NSF for support of GIMNAST through grant AGS-1004736. Thumbnail summaries of THEMIS ASI data are available online (http://themis.ssl.berkeley.edu/gbo/display.py). Specific intervals of THEMIS ASI data are automatically downloaded from the themis.ssl.berkeley.edu site by using the purpose-built software package SPEDAS. This is part of the THEMIS Data Analysis Software (http://themis.ssl.berkeley.edu/software.shtml). K_P data are part of the Daily Geomagnetic Data provided by the U.S. Dept. of Commerce, NOAA, Space Weather Prediction Center (http://www.swpc.noaa.gov/products/planetary-k-index). We acknowledge use of the United States (U.S.) Navy data service to obtain Astronomical Twilight times (http://aa.usno.navy.mil/data/docs/RS_OneYear.php). The SML index is available online (supermag.jhuapl.edu). With regard to the use of SML data derived from ground magnetometer data, we gratefully acknowledge Intermagnet; USGS, Jeffrey J. Love; CARISMA, PI Ian Mann; CANMOS; The S-RAMP Database, PI K. Yumoto and Dr. K. Shiokawa; The SPIDR database; AARI, PI Oleg Troshichev; The MACCS program, PI M. Engebretson, Geomagnetism Unit of the Geological Survey of Canada; GIMA; MEASURE, UCLA IGPP and Florida Institute of Technology; SAMBA, PI Eftyhia Zesta; 210 Chain, PI K. Yumoto; SAMNET, PI Farideh Honary; The institutes who maintain the IMAGE magnetometer array, PI Eija Tanskanen; PENGUIN; AUTUMN, PI Martin Connors; DTU Space, PI Dr Rico Behlke; South Pole and McMurdo Magnetometer, PI's Louis J. Lanzarotti and Alan T.

References

Aikio, A. T., & Kaila, K. U. (1996). A substorm observed by EISCAT and other ground-based instruments—Evidence for near-Earth substorm initiation. *Journal of Atmospheric and Terrestrial Physics*, *58*(1–2), 5–21. https://doi.org/10.1016/0021-9169(95)00016-X

Aikio, A. T., & Selkälä, A. (2009). Statistical properties of Joule heating rate, electric field and conductances at high latitudes. *Annales de Geophysique*, *27*(7), 2661–2673. https://doi.org/10.5194/angeo-27-2661-2009

Bartels, J. (1949). The standardized index, Ks, and the planetary index, Kp. *IATME Bulletin*, *12B*, 109.

Bilitza, D. (1990). International Reference Ionosphere: IRI-90, http://nssdc.gsfc.nasa.gov, Nat. Space Sci. Data Cent., *Rep. 90–22*, Greenbelt, Md.

Clilverd, M. A., Rodger, C. J., Rae, I. J., Brundell, J. B., Thomson, N. R., Cobbett, N., et al. (2012). Combined THEMIS and ground-based observations of a pair of substorm-associated electron precipitation events. *Journal of Geophysical Research*, *117*, A02313. https://doi.org/10.1029/2011JA016933

Craven, J. D., Frank, L. A., & Akasofu, S.-I. (1989). Propagation of a westward traveling surge, and development of persistent auroral features. *Journal of Geophysical Research*, *94*(A6), 6961–6967. https://doi.org/10.1029/JA094iA06p06961.

Davies, J. A., & Lester, M. (1999). The relationship between electric fields, conductances and currents in the high-latitude ionosphere: A statistical study using EISCAT data. *Annales Geophysicae*, *17*(1), 43–52.

Gjerloev, J. W. (2012). The SuperMAG data processing technique. *Journal of Geophysical Research*, *117*, A09213. https://doi.org/10.1029/2012JA017683

Hargreaves, J. K. (1979). *The upper atmosphere and solar-terrestrial relations*. New York: Van Nostrand Reinhold Company.

Huuskonen, A., Lehtinen, M. S., & Pirttilä, J. (1996). Fractional lags in alternating codes: Improving incoherent scatter measurements by using lag estimates at noninteger multiples of baud length. *Radio Science*, *31*(2), 245–261. https://doi.org/10.1029/95RS03157

Kaeppler, S. R., Hampton, D. L., Nicolls, M. J., Strømme, A., Solomon, S. C., Hecht, J. H., & Conde, M. G. (2015). An investigation comparing ground-based techniques that quantify auroral electron flux and conductance. *Journal of Geophysical Research: Space Physics*, *120*, 9038–9056. https://doi.org/10.1002/2015JA021396

Kamide, Y., Richmond, A. D., & Matsushita, S. (1981). Estimation of ionospheric electric fields, ionospheric currents, and field-aligned currents from ground magnetic records. *Journal of Geophysical Research*, *86*(A2), 801–813. https://doi.org/10.1029/JA086iA02p00801

Kelly, J. D., & Heinselman, C. J. (2009). Initial results from Poker Flat Incoherent Scatter Radar (PFISR). *Journal of Atmospheric and Solar - Terrestrial Physics*, *71*(6–7), 635–635. https://doi.org/10.1016/j.jastp.2009.01.009

Kirkwood, S., Opgenoorth, H., & Murphree, J. S. (1988). Ionospheric conductivities, electric fields and currents associated with auroral substorms measured by the EISCAT radar. *Planetary and Space Science*, *36*(12), 1359–1380. https://doi.org/10.1016/0032-0633(88)90005-0

Knipp, D. J., Welliver, T., McHarg, M. G., Chun, F. K., Tobiska, W. K., & Evans, D. (2005). Climatology of extreme upper atmospheric heating events. *Advances in Space Research*, *36*(12), 2506–2510. https://doi.org/10.1016/j.asr.2004.02.019.

Kosch, M. J., Hagfors, T., & Schlegel, K. (1998). Extrapolating EISCAT Pedersen conductances to other parts of the sky using ground-based TV auroral images. *Annales de Geophysique*, *16*(5), 583–588. https://doi.org/10.1007/s00585-998-0583-y

Lester, M., Davies, J. A., & Virdi, T. S. (1996). High-latitude Hall and Pedersen conductances during substorm activity in the SUNDIAL-ATLAS campaign. *Journal of Geophysical Research*, *101*(A12), 26719–26728. https://doi.org/10.1029/96JA00979

Mende, S. B., Frey, H. U., Angelopoulos, V., & Nishimura, Y. (2011). Substorm triggering by poleward boundary intensification and related equatorward propagation. *Journal of Geophysical Research*, *116*, A00131. https://doi.org/10.1029/2010JA015733

Mende, S. B., Harris, S. E., Frey, H. U., Angelopoulos, V., Russell, C. T., Donovan, E., et al. (2008). The THEMIS array of ground-based observatories for the study of auroral substorms. *Space Science Reviews*, *141*(1-4), 357–387. https://doi.org/10.1007/s11214-008-9380-x

Murphy, K. R., Rae, I. J., Mann, I. R., & Milling, D. K. (2011). On the nature of ULF wave power during nightside auroral activations and substorms: 1. Spatial distribution. *Journal of Geophysical Research*, *116*, A00I21. https://doi.org/10.1029/2010JA015757

Newell, P. T., & Gjerloev, J. W. (2011). Evaluation of SuperMAG auroral electrojet indices as indicators of substorms and auroral power. *Journal of Geophysical Research*, *116*, A12211. https://doi.org/10.1029/2011JA016779

Nicolls, M. J., Heinselman, C. J., Hope, E. A., Ranjan, S., Kelley, M. C., & Kelly, J. D. (2007). Imaging of polar mesosphere summer echoes with the 450 MHz poker flat advanced modular incoherent scatter radar. *Geophysical Research Letters*, *34*, L20102. https://doi.org/10.1029/2007GL031476

Weatherwax; ICESTAR; RAPIDMAG; PENGUIn; British Antarctic Survey; McMac, PI Dr Peter Chi; BGS, PI Dr Susan Macmillan; Pushkov Institute of Terrestrial Magnetism, Ionosphere and Radio Wave Propagation (IZMIRAN); GFZ, PI Dr Juergen Matzka; MFGI, PI B. Heilig; IGFPAS, PI J. Reda; University of L'Aquila, PI M. Vellante; BCMT, V. Lesur and A. Chambodut; Data obtained in cooperation with Geoscience Australia, PI Marina Costelloe; SuperMAG, PI Jesper W. Gjerloev.

Østgaard, N., Germany, G., Stadsnes, J., & Vondrak, R. R. (2002). Energy analysis of substorms based on remote sensing techniques, solar wind measurements, and geomagnetic indices. *Journal of Geophysical Research*, *107*(A9), 1233. https://doi.org/10.1029/2001JA002002

Picone, J. M., Hedin, A. E., Drob, D. P., & Aikin, A. C. (2002). NRLMSISE-00 empirical model of the atmosphere: Statistical comparisons and scientific issues. *Journal of Geophysical Research*, *107*(A12), 1468. https://doi.org/10.1029/2002JA009430

Rae, I. J., Watt, C. E. J., Fenrich, F. R., Mann, I. R., Ozeke, L. G., & Kale, A. (2007). Energy deposition in the ionosphere through a global field line resonance. *Annales de Geophysique*, *25*(12), 2529–2539. https://doi.org/10.5194/angeo-25-2529-2007

Richards, P. G. (2011). Reexamination of ionospheric photochemistry. *Journal of Geophysical Research*, *116*, A08307. https://doi.org/10.1029/2011JA016613

Schunk, R. W., & Nagy, A. F. (1978). Electron temperatures in the F region of the ionosphere: Theory and observations. *Reviews of Geophysics and Space Physics*, *16*(3), 355–399. https://doi.org/10.1029/RG016i003p00355

Schunk, R. W., & Walker, J. C. G. (1973). Theoretical ion densities in the lower ionosphere. *Planetary and Space Science*, *21*(11), 1875–1896. https://doi.org/10.1016/0032-0633(73)90118-9

Senior, A., Kavanagh, A. J., Kosch, M. J., & Honary, F. (2007). Statistical relationships between cosmic radio noise absorption and ionospheric electrical conductances in the auroral zone. *Journal of Geophysical Research*, *112*, A11301. https://doi.org/10.1029/2007JA012519

Senior, A., Kosch, M. J., & Honary, F. (2008). Comparison of methods to determine auroral ionospheric conductances using ground-based optical and riometer data. *Annales de Geophysique*, *26*(12), 3831–3840. https://doi.org/10.5194/angeo-26-3831-2008

Shore, R. M., Freeman, M. P., Wild, J. A., & Gjerloev, J. W. (2017). A high-resolution model of the external and induced magnetic field at the Earth's surface in the Northern Hemisphere. *Journal of Geophysical Research: Space Physics*, *122*, 2440–2454. https://doi.org/10.1002/2016JA023682

Uritsky, V. M., Klimas, A. J., Vassiliadis, D., Chua, D., & Parks, G. (2002). Scale-free statistics of spatiotemporal auroral emissions as depicted by POLAR UVI images: Dynamic magnetosphere is an avalanching system. *Journal of Geophysical Research*, *107*(A12), 1426. https://doi.org/10.1029/2001JA000281

Vickrey, J. F., Vondrak, R. R., & Matthews, S. J. (1981). The diurnal and latitudinal variation of auroral zone ionospheric conductivity. *Journal of Geophysical Research*, *86*(A1), 65–75. https://doi.org/10.1029/JA086iA01p00065

Wallis, D. D., & Budzinski, E. E. (1981). Empirical models of height integrated conductivities. *Journal of Geophysical Research*, *86*(A1), 125–137. https://doi.org/10.1029/JA086iA01p00125

Zettergren, M., Semeter, J., Burnett, B., Oliver, W., Heinselman, C., Blelly, P.-L., & Diaz, M. (2010). Dynamic variability in F-region ionospheric composition at auroral arcboundaries. *Annales de Geophysique*, *28*(2), 651–664. https://doi.org/10.5194/angeo-28-651-2010.

Zou, S., Lyons, L. R., Nicolls, M. J., Heinselman, C. J., & Mende, S. B. (2009). Nightside ionospheric electrodynamics associated with substorms: PFISR and THEMIS ASI observations. *Journal of Geophysical Research*, *114*, A12301. https://doi.org/10.1029/2009JA014259

Zou, S., Ozturk, D., Varney, R., & Reimer, A. (2017). Effects of sudden commencement on the ionosphere: PFISR observations and global MHD simulation. *Geophysical Research Letters*, *44*, 3047–3058. https://doi.org/10.1002/2017GL072678